Rate-dependent intra-ply shear of woven CF/PA6: Characterisation and modelling for thermoforming

Chunyi Gao[1], Haibao Liu[2], Bamber Blackman[3], Nan Li[1] *

[1]Dyson School of Design Engineering, Imperial College London, London, UK

[2] School of Engineering and Materials Science, Queen Mary University of London, London, UK

[3] Department of Mechanical Engineering, Imperial College London, London, UK

*Corresponding author: nan.li@imperial.ac.uk

Abstract

This work develops a rate-dependent intra-ply shear model for molten woven carbon-fibre/polyamide 6 (CF/PA6) from bias-extension testing and validates it in U-shaped thermoforming. Tests were conducted from 190 to 270 °C, with five deformation rates at 230 °C and three specimens per condition. Below the PA6 melting peak, measured yarn rotation departed from the analytical bias-extension relation. Above the melting peak, measured and analytical shear angles remained close over 0–14 mm displacement, corresponding to an analytical shear angle of 39.7°. Across the tested molten-state temperatures, deformation rate produced a clearer effect on shear response than temperature. A continuous two-branch law was developed using shear angle and local engineering shear rate and fitted simultaneously to the five rate conditions. The model reproduced the measured shear response with a pooled RMSE of 0.0103 MPa and $R^2 = 0.966$ over 0–14 mm displacement. The law was implemented through VUMAT as the nonlinear 12-shear response of three-dimensional solid elements in a 15-ply U-shaped thermoforming model. Validation against surface yarn-angle measurements from two forming tests showed that the numerical profile reproduced the main centreline shear-angle variation across nine locations, with a mean absolute error of 1.89° and a root-mean-square error of 2.21°.

Keywords: woven thermoplastic composites; bias-extension test; intra-ply shear; thermoforming

1 Introduction

Fibre-reinforced thermoplastic composites are increasingly used in lightweight structures because they can be heated, formed and consolidated within short processing cycles [1, 2]. Stamp forming is a key manufacturing route for these materials, and the quality of the formed component depends on how the laminate accommodates deformation during tool closure [3]. The main deformation mechanisms include intra-ply tension and shear, inter-ply sliding and bending [4–8]. In woven plies, intra-ply shear is particularly important for complex and double-curved geometries because it enables yarn rotation and local material rearrangement without large fibre stretching [9]. Reliable forming analysis therefore requires these deformation mechanisms to be characterised separately before they are incorporated into numerical models [10, 11].

Woven CF/PA6 was selected because its woven carbon-fibre architecture and semi-crystalline PA6 matrix provide both the yarn-rotation mechanism typical of woven composites and a clear transition between solid and molten processing states [12–15]. During forming, the initially orthogonal warp and weft yarns mainly accommodate in-plane deformation through yarn rotation. As the shear angle increases, yarn rotation becomes increasingly restricted by tow contact, local compaction and geometric locking [16]. Below the melting temperature, the PA6 matrix restricts yarn rotation and increases shear resistance. Above the melting temperature, greater yarn mobility is enabled, while the molten matrix introduces deformation-rate-dependent viscous resistance [17].

Intra-ply shear behaviour is commonly characterised using the picture-frame test and the bias-extension test (BET) [15, 18–20]. The picture-frame test can produce a relatively uniform shear state when the specimen is mounted accurately within a hinged frame. However, the measured response can be affected by frame alignment, yarn misalignment, local clamping effects and friction between the specimen and the frame [18, 20]. These effects are more difficult to control when thermoplastic prepregs are tested at elevated temperatures. The bias-extension test uses a rectangular specimen with the yarns initially oriented at ±45° to the loading direction. During loading, the specimen develops distinct deformation zones with different shear levels. Under ideal BET kinematics, the central region undergoes approximately uniform pure shear, allowing the shear angle to be related to crosshead displacement [19, 20]. This configuration is well suited to elevated-temperature testing and is widely used to characterise the in-plane shear response of thermoplastic prepregs [11, 21].

Previous studies have shown that the shear behaviour of thermoplastic composites is affected by both matrix thermal state and deformation rate. Street and Johnson [22] investigated non-isothermal intra-ply shear in woven CF/PA6 and reported decreasing shear resistance as the temperature approached the molten range, without considering rate effects. Zomer et al. [23] observed clear rate dependence in cross-ply unidirectional (UD) CF/PA6, although its deformation mechanism differs from yarn rotation in woven plies. Abadi et al. [24] investigated temperature- and rate-dependent shear behaviour of spread-tow woven flax-fibre/polypropylene (Flax/PP) laminates using elevated-temperature bias-extension testing and finite element modelling. Machado et al. [21] characterised the temperature- and rate-dependent shear response of woven glass-fibre/polypropylene (GF/PP) and applied the measured behaviour in forming analysis. A related non-orthogonal constitutive model included shear-angle and rate dependence and was assessed using a forming experiment [25]. These studies demonstrate the importance of temperature and rate effects in thermoplastic-composite shear modelling and forming analysis.

For woven CF/PA6, rate-dependent molten-state intra-ply shear and its use in forming simulation have received limited attention. This work develops a rate-dependent intra-ply shear model for molten woven CF/PA6 from bias-extension testing and validates it in U-shaped thermoforming. The main contributions are summarised as follows:

- Characterisation of thermal-state and deformation-rate effects on woven CF/PA6 shear behaviour, including assessment of the valid bias-extension kinematic range;
- Development and three-dimensional VUMAT implementation of a continuous two-branch rate-dependent shear law;
- Validation of the model against centreline yarn-angle measurements in a 15-ply U-shaped thermoforming case.

The remainder of this paper is organised as follows. Section 2 describes the experimental methods, Section 3 presents the bias-extension results, Section 4 develops the constitutive model and VUMAT implementation, Section 5 presents the U-shaped thermoforming validation, and Sections 6 and 7 provide the discussion and conclusions, respectively.

2 Materials and experimental methods

The material used in this study was a woven carbon-fibre-reinforced polyamide 6 prepreg, Tepex® dynalite 202-C200(x)/45%, supplied by Bond-Laminates [26]. It has a 2/2 twill woven carbon-fibre architecture

with PA6 as the thermoplastic matrix. The dry-fabric areal weight is 200 g m^{-2}, the fibre volume content is 45%, and the ply thickness is 0.25 mm. A single prepreg ply was used in the bias-extension tests to isolate the intra-ply shear response and avoid additional effects from inter-ply sliding or laminate-level deformation. The manufacturer-provided material data are summarised in Table 1.

Table 1 Manufacturer-reported properties of the woven CF/PA6 prepreg.

	Properties	Value
Reinforcement		
	Fibre	3K Carbon
	Weave style	Twill 2/2
	Dry-fabric areal weight	200 g m^{-2}
	Warp/weft areal-weight ratio	50/50
Matrix		
	Polymer	Polyamide 6 (PA6)
Composite		
	Fibre volume content	45 vol.%
	Ply thickness	0.25 mm
	Density	1420 kg m^{-3}

2.1 Thermal characterisation

Differential scanning calorimetry (DSC) was performed to characterise the thermal transitions of the PA6 matrix in the woven CF/PA6 prepreg. Measurements were conducted using a TA Discovery DSC 250 with a sample mass of approximately 15 mg. The specimen was heated from 0 °C to 300 °C at 10 K min^{-1} and then cooled to 0 °C at the same rate. Heat flow was defined as positive in the exothermic direction. Figure 1 shows a melting peak at approximately 221.2 °C during heating and a crystallisation peak at approximately 189.1 °C during cooling. These temperatures were used to guide the selection of the below-melting, transition and molten-state conditions for the bias-extension tests.

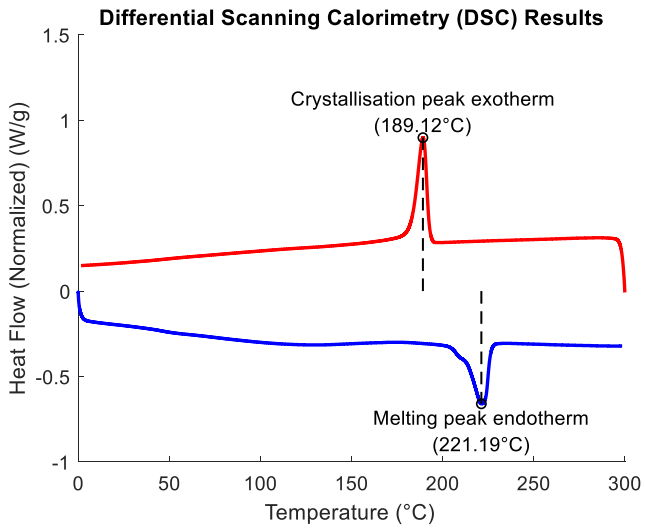


Figure 1 Differential scanning calorimetry (DSC) curve of the woven CF/PA6 prepreg.

2.2 Bias-extension test setup and conditions

Bias-extension specimens were prepared from single-ply woven CF/PA6 prepreg by waterjet cutting. The specimens had a total length of 160 mm and an initial width of 50 mm. Approximately 30 mm at each end was clamped, giving a free length of 100 mm between the grips. The warp and weft yarns were initially oriented at ±45° to the loading direction. The specimen geometry and deformation zones are shown in Figure 2a, with representative specimen states before and during deformation shown in Figure 2b. Boundary lines were marked on the specimen surface to identify the deformation zones and support subsequent shear-angle measurement. After cutting, the specimens were surface-dried with a hot-air gun for approximately 3–5 min at an estimated 60–70 °C and stored in sealed bags under ambient laboratory conditions prior to testing, which was completed within two weeks.

The experimental setup is shown in Figure 2c,d. Tests were performed on an Instron 5584 universal testing machine equipped with a 10 kN load cell. Screw side-action tensile grips were used to clamp the specimens inside a temperature-controlled chamber. Before loading, each specimen was held at the test temperature for 20 min to allow thermal stabilisation. Thermocouples were placed near both ends of the specimen to monitor temperature during testing. The lower grip was fixed, while the upper grip was displaced upwards at the selected crosshead speed. Load and crosshead displacement were recorded by the testing machine, with machine compliance checked before each test. A Canon high-speed camera recorded specimen deformation for subsequent yarn-angle measurement.

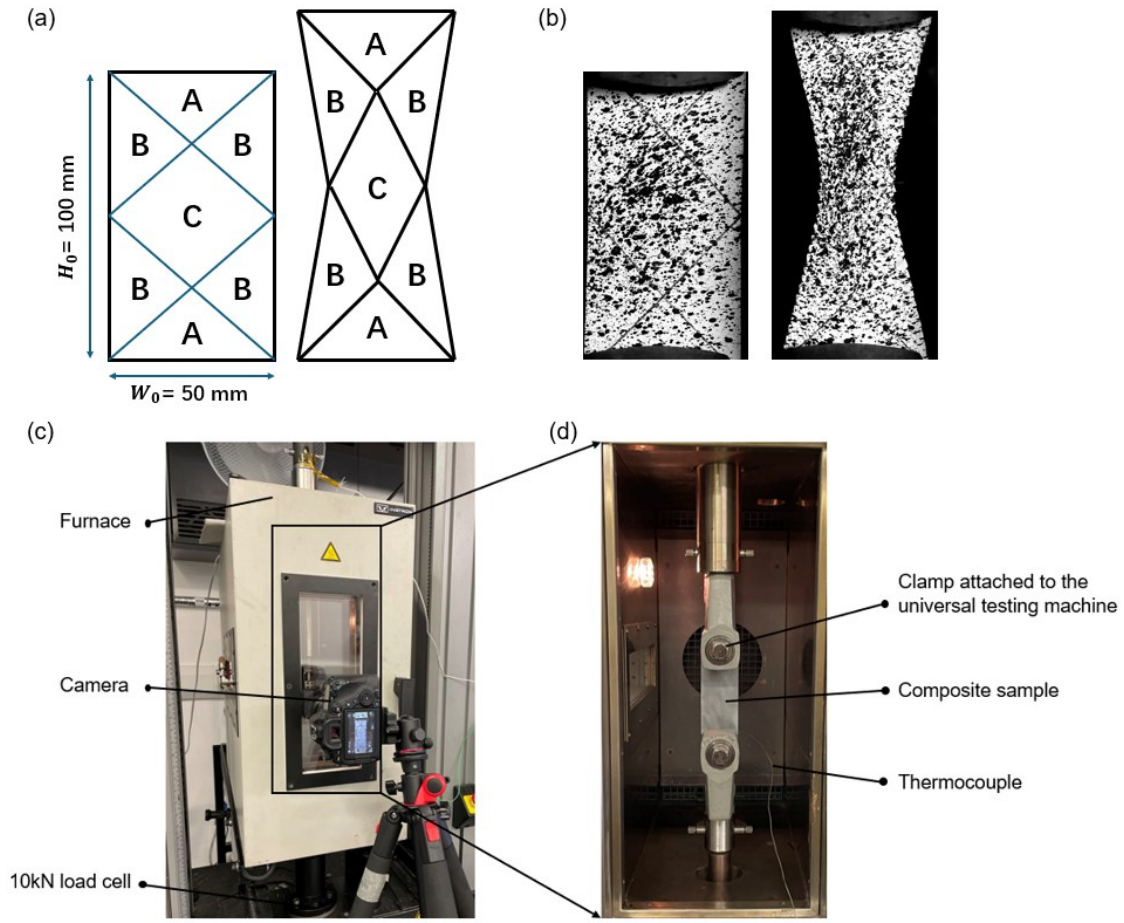


Figure 2 Bias-extension specimen and experimental setup: (a) specimen geometry and deformation zones; (b) prepared specimen before and during deformation; (c) overall experimental setup; (d) specimen and gripping arrangement inside the temperature-controlled chamber. The specimen had a total length of 160 mm, a free length of 100 mm and an initial width of 50 mm.

The test matrix was designed to examine the effects of matrix thermal state and deformation rate on the bias-extension response. The deformation rate was calculated from the crosshead speed divided by the 100 mm free length. Based on the DSC results, five temperatures were selected: 190, 210, 230, 250 and 270 °C, covering the below-melting, transition and molten states of the PA6 matrix. For the temperature-dependence study, tests were conducted at a fixed deformation rate of 0.01 s^{-1}, corresponding to a crosshead speed of 60 mm min^{-1}. For the rate-dependence study, tests were conducted at 230 °C using crosshead speeds of 6, 30, 60, 300 and 500 mm min^{-1}, corresponding to deformation rates of 0.001, 0.005, 0.010, 0.050 and 0.083 s^{-1}, respectively. Three specimens were tested for each condition. The full test matrix is summarised in Table 2.

Table 2 Bias-extension test matrix for the temperature- and rate-dependence studies. Three specimens were tested for each condition.

Temperature (°C)	**Deformation rate (s^{-1})**				
	0.001	0.005	0.010	0.050	0.083
190			√		
210			√		
230	√	√	√	√	√
250			√		
270			√		

2.3 Shear-angle determination

The standard bias-extension analysis [19, 20] was followed. The specimen is divided into regions A, B and C (Figure 2a), where region A remains undeformed, region B undergoes intermediate shear, and region C undergoes the largest shear deformation. Under the pin-jointed-net assumption, the shear angle in region C is approximately twice that in region B, with yarn rotation occurring at the crossover points without in-plane fibre stretching or yarn slippage [19, 20]. Region C was used for yarn-angle measurement and bias-extension data reduction.

The shear angle in region C was measured from the recorded specimen images. The marked boundary lines were used as references to track yarn rotation during deformation. Yarn angles were measured frame by frame in MATLAB, with the video time matched to the machine records to obtain the load and displacement at each frame. The analytical shear angle was calculated from the Lebrun bias-extension relation using the specimen dimensions and crosshead displacement [19].

The analytical shear angle in region C can be expressed as:

$$\gamma = \frac{\pi}{2} - 2cos^{-1}\left(\frac{(H_0+\delta)-W_0}{2(H_0-W_0)\,cos\left(\frac{\pi}{4}\right)}\right), \tag{1}$$

where H_0 and W_0 are the initial free length (100 mm) and initial width (50 mm), respectively, δ is the crosshead displacement in mm, and γ is the region-C shear angle in radians. The analytical angle was evaluated in radians for strain and strain-rate conversion and converted to degrees for presentation.

The local engineering shear strain and shear rate in region C were calculated as

$$\gamma_{12} = \tan\gamma,\ \dot{\gamma}_{12} = \sec^2\gamma \mid \frac{\mathrm{d}\gamma}{\mathrm{d}\delta} \mid v, \tag{2}$$

where $v = d\delta/dt$ is the crosshead speed, γ_{12} is the dimensionless engineering 12-shear strain, and $\dot{\gamma}_{12}$ is the local engineering shear rate in s^{-1}. The derivative $d\gamma/d\delta$ was evaluated with γ in radians.

2.4 Shear-force and shear-stress calculation

The measured axial force was converted to normalised shear force per unit length using the viscous bias-extension normalisation proposed by Harrison et al. [15]. This formulation accounts for the contributions of the different deformation regions using a constrained Newtonian-viscous approximation [27, 28]:

$$F_{\mathrm{sh}}(\gamma) = \left(\frac{H_0/W_0 - 1}{2H_0/W_0 - 3 + 2X}\right)\frac{\sqrt{2}F}{W_0}, \tag{3}$$

where F is the measured axial force in N, F_{sh} is the normalised shear force per unit length in N mm^{-1}, and X is a dimensionless geometric correction factor evaluated using the analytical region-C shear angle [15]:

$$X = \frac{1}{4}\left(\frac{\cos^2\gamma}{\cos^2(\gamma/2)}\right)\left(\frac{1+3\sin^2(\gamma/2)}{1+3\sin^2\gamma}\right). \tag{4}$$

The shear stress was obtained by dividing F_{sh} by the ply thickness:

$$\tau = \frac{F_{\mathrm{sh}}}{t}, \tag{5}$$

where t is the ply thickness of 0.25 mm.

2.5 U-shaped thermoforming experiments

The U-shaped forming experiments used a consolidated woven CF/PA6 laminate with 15 identically oriented plies, with the warp and weft yarns at ±45° to the blank length ($[45°]_{15}$). The prepregs were stacked in a custom mould and consolidated using an MSE LP_M4SH50 manual hot press. During heating, the mould temperature was increased to 255 °C under 5 bar. The pressure was then increased to 11 bar and held for 20 min. The laminate was cooled under pressure to approximately 190 °C, followed by water cooling to below 40 °C before demoulding. The consolidated panel was waterjet-cut into 120 × 40 × 3 mm blanks. Two blanks were formed under the same conditions.

Before forming, the blanks were heated at a furnace set point of 275 °C for 10 min, reaching a measured temperature of approximately 265–270 °C. Blank temperature was monitored using embedded K-type thermocouples. The heated blank was then transferred to an ESH 25T high-rate forming machine and positioned between the die and blank holder. The transfer time to tool contact was approximately 3.5 s, during which the blank temperature decreased to approximately 245 °C. This temperature was used to initialise the numerical model. Figure 3 shows the forming system and U-shaped tool assembly. The die, punch, blank holder and spacers were made from heat-treated H13 steel and were at room temperature during forming.

The blank-holding force was 60 kN, the forming speed was 100 mm s^{-1}, and the laminate was held under tool closure for 30 s before unloading. The spacers controlled the final tool gap and limited excessive through-thickness compression. The same forming and holding conditions were used in the numerical model described in Section 5.

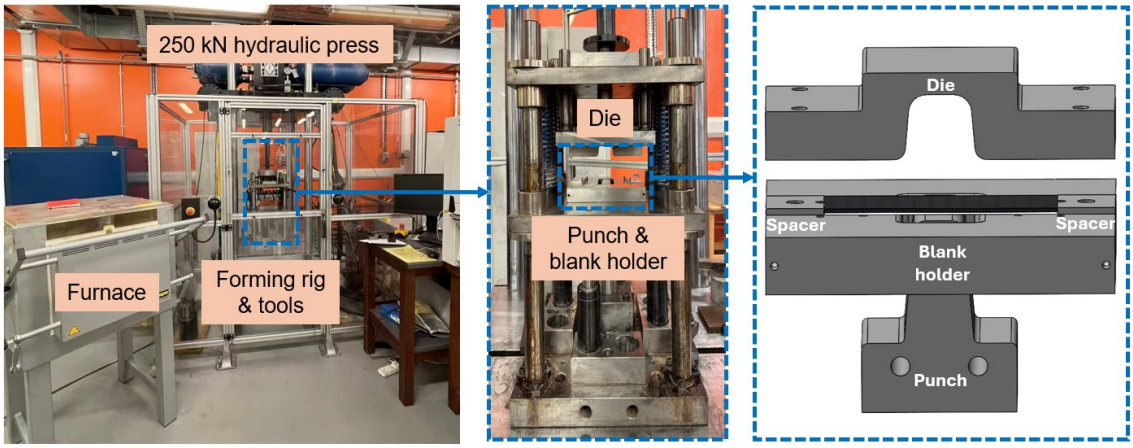


Figure 3 U-shaped thermoforming setup and tool assembly.

2.6 Experimental forming assessment

After unloading, side-view and surface photographs were acquired using a Fujifilm X-S20 digital camera under shadowless illumination. The side views were used to assess the overall formed geometry and corner conformity. Cross-sectional optical micrographs were obtained from the upper-corner and wall regions using a Leica DMi8 optical microscope at 10× magnification to examine the local reinforcement morphology.

Surface yarn rotation was measured along a fixed centreline path on the outer surface of the formed laminate. The path was located at the mid-width of the outermost woven ply and extended from the top flange, through the upper corner and wall, to the lower corner and lower flange. Experimental measurement locations were identified from the surface photographs. Position along the path was denoted by s, measured along the formed surface from $s = 0$ at the top-flange end.

For surface yarn-angle measurement, the camera was positioned approximately normal to the local laminate surface to minimise perspective distortion. The included angle, β, between the local warp and weft directions was measured from the surface images, and the shear angle was calculated as

$$\theta_{\mathrm{exp}} = | 90^{\circ} - \beta |, \tag{6}$$

where θ_{exp} is the measured shear angle in degrees. Nine measurement locations were identified in each of the two forming tests, and the values from the two tests were reported separately.

3 Bias-extension response across thermal states and rates

This section establishes the experimental basis for the constitutive model. The measured and analytical shear-angle histories are first compared to assess how matrix thermal state affects the bias-extension deformation mode. The load–displacement response is then examined to identify the main response regimes. Finally, the effects of temperature and deformation rate on the normalised shear force and shear stress are evaluated. Together, these results define the molten-state, rate-dependent dataset used to calibrate the model in Section 4.

3.1 Shear-angle analysis

Figure 4 compares the measured shear-angle histories in region C with the analytical prediction from Eq. (1), the Lebrun relation. At a deformation rate of 0.010 s^{-1}, the measured histories at 190 and 210 °C differed from the analytical curve, whereas those at 230, 250 and 270 °C remained close to it up to approximately 14 mm of crosshead displacement. At 14 mm, the analytical shear angle is 39.7°, as indicated by the dashed guides in Figure 4. The four additional tests at 230 °C showed similar early angle evolution at the other deformation rates. Beyond 14 mm, the molten-state histories progressively departed from the analytical relation.

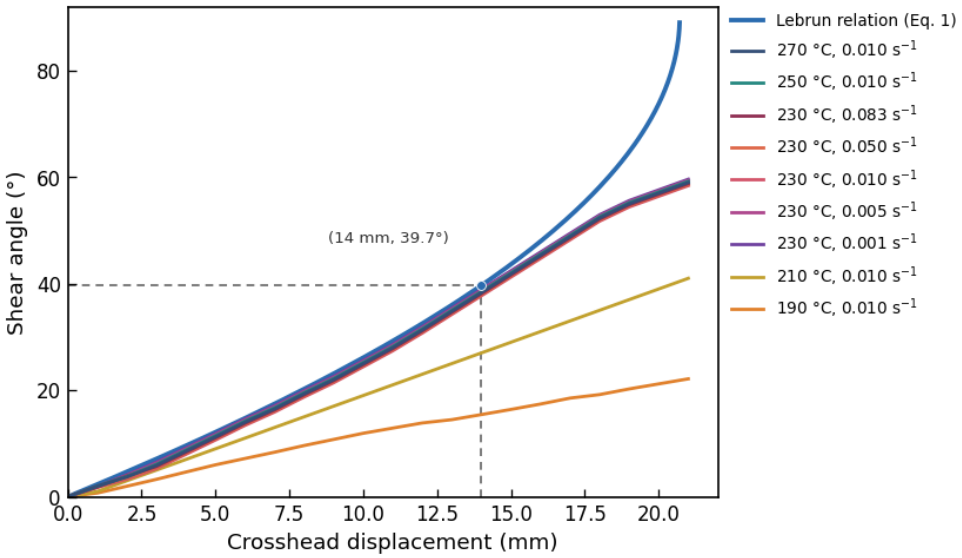
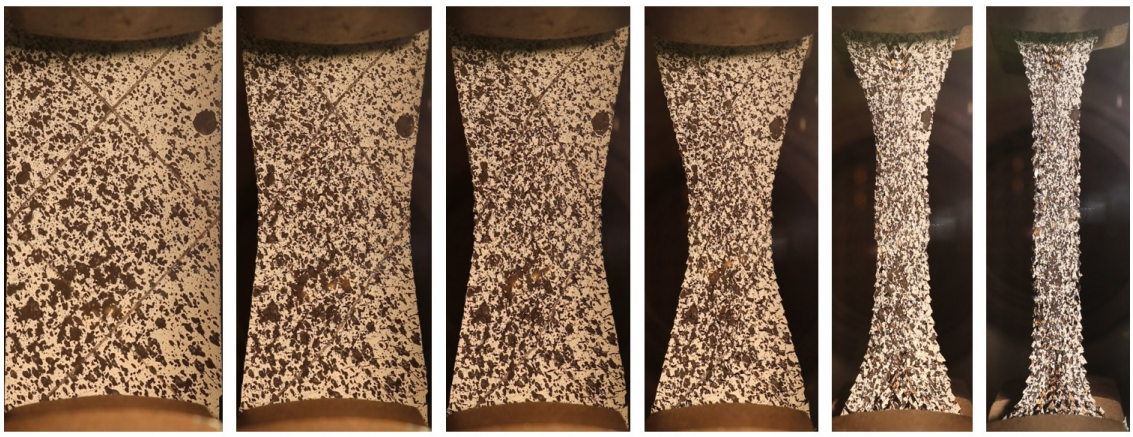


Figure 4 Shear-angle evolution in region C during bias-extension testing. The blue curve shows the analytical prediction from Eq. (1), the Lebrun relation. Each coloured curve represents one measured specimen: five temperatures at a deformation rate of 0.010 s^{-1} and four additional rates at 230 °C. The dashed guides mark 14 mm displacement and the analytical shear angle of 39.7°.

Clear differences between the measured and analytical shear angles were observed at 190 and 210 °C. At these temperatures, the PA6 matrix remained below the melting peak and restricted yarn rotation, leading to greater deviation from the ideal bias-extension response. The measured deformation may therefore include non-shear and non-uniform components. In contrast, the specimens tested at 230, 250 and 270 °C showed similar shear-angle evolution, with the measured angles remaining close to the analytical relation over the early deformation range.

Figure 5 shows representative deformation images for a specimen tested at 230 °C and 0.01 s^{-1}. The specimen deformed symmetrically during the early stage of loading, with clear narrowing near the centre of the gauge region. Limited grip slippage was observed throughout this stage. Up to a displacement of 14 mm (Figure 5c), the deformation remained close to the ideal bias-extension mode, with narrowing mainly concentrated in the central region. This agrees with the measured and analytical shear-angle histories in Figure 4. At a displacement of 20 mm (Figure 5d), the deformation began to spread along the specimen length and the shape deviated from the ideal bias-extension pattern. This is consistent with the shear-angle deviation observed beyond 14 mm in Figure 4. With further displacement, the deformation became increasingly non-uniform, with more evident tow interaction, yarn slip and geometric constraint. At the end of the test (Figure 5f), only part of the specimen continued to deform through the ideal shear mode, while

other regions retained a nearly constant width. These observations separate the early ideal bias-extension response from the later non-uniform deformation.



(a) (b) (c) (d) (e) (f)

Figure 5 Snapshots of the specimen during bias-extension testing at different displacements: (a) 0 mm, (b) 10 mm, (c) 14 mm, (d) 20 mm, (e) 30 mm, and (f) 40 mm.

Figure 6 shows four regimes in the load–displacement responses above the PA6 melting peak. In Regime 1, the force rises rapidly at the start of loading as the yarns begin to rotate and rearrange. Tow interaction and resistance from the molten matrix contribute to the initial response. In Regime 2, the force changes more gradually as deformation is mainly accommodated by yarn rotation. The measured shear angles in region C remain close to the analytical prediction up to approximately 14 mm displacement (Figure 4), consistent with the specimen deformation shown in Figure 5.

In Regime 3, the force rises towards a maximum near 35 mm, with the steepest increase occurring at approximately 20–30 mm. Continued yarn rotation increases tow interaction and local compaction, progressively restricting further shear. The resulting increase in resistance is consistent with the development of shear locking in woven textiles [15, 18]. The measured shear angles begin to depart from the analytical prediction beyond approximately 14 mm, before the steepest force increase. In Regime 4, the force decreases as deformation becomes concentrated in a narrower part of the specimen (Figure 5). Yarn slip, tow separation and the changing specimen geometry may all contribute to the later force reduction.

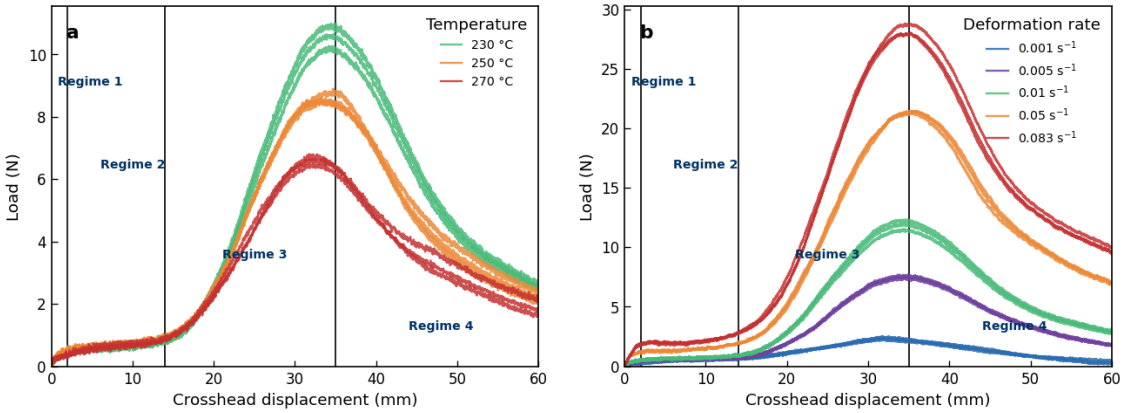


Figure 6 Load–displacement responses above the PA6 melting peak: (a) effect of temperature at a deformation rate of 0.01 s^{-1}; (b) effect of deformation rate at 230 °C. Three individual specimen curves are shown for each condition. Regimes 1–4 indicate successive parts of the load response.

3.2 Effect of temperature on shear behaviour

Figure 7 shows the load–displacement responses at a deformation rate of 0.01 s^{-1}. The load decreases markedly as the temperature increases across the PA6 melting range. The load at 190 °C is much higher than at the other temperatures, while the response at 210 °C remains clearly above those at 230, 250 and 270 °C. This behaviour is consistent with greater resistance to yarn rotation below the PA6 melting peak. The load responses can be considered together with the shear-angle histories in Figure 4. At 190 and 210 °C, the measured angles depart from the analytical bias-extension relation, showing that the deformation differs from the ideal shear mode. At 230, 250 and 270 °C, the measured angles remain close to the analytical relation over the early deformation range. Figure 8 compares the reduced shear responses at these three molten-state temperatures.

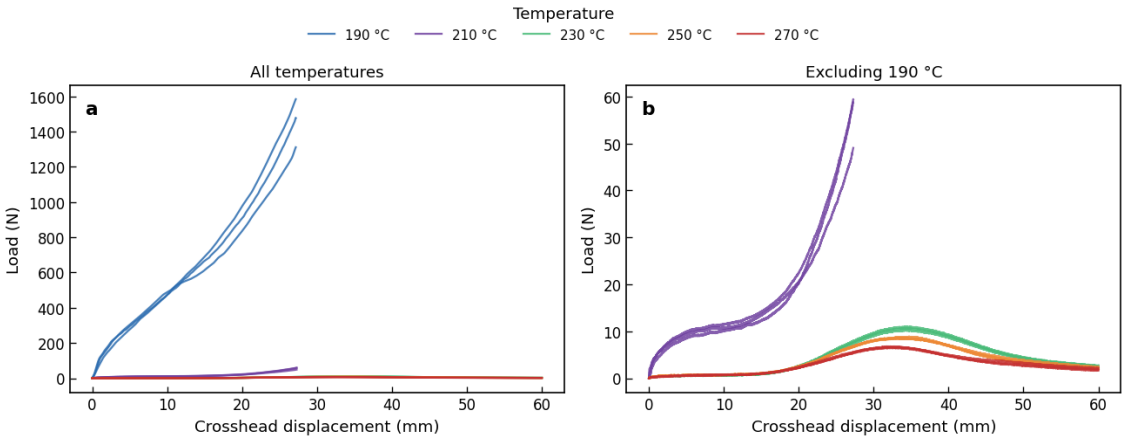


Figure 7 Load–displacement responses of woven CF/PA6 specimens tested at 0.01 s^{-1} at different temperatures: (a) all temperatures; (b) enlarged view excluding 190 °C. Three individual specimen curves are shown for each temperature.

Figure 8 compares the molten-state shear responses at 230, 250 and 270 °C. The normalised shear force and shear stress remain closely grouped across the three temperatures over most of the shear-angle range. No consistent increase or decrease with temperature is observed, and the relative ordering of the curves changes slightly with shear angle.

Some separation develops at larger shear angles, but the differences among the three temperatures remain small compared with the change across the PA6 melting range shown in Figure 7. These results indicate that temperature has a limited effect on the molten-state shear response between 230 and 270 °C under the tested condition.

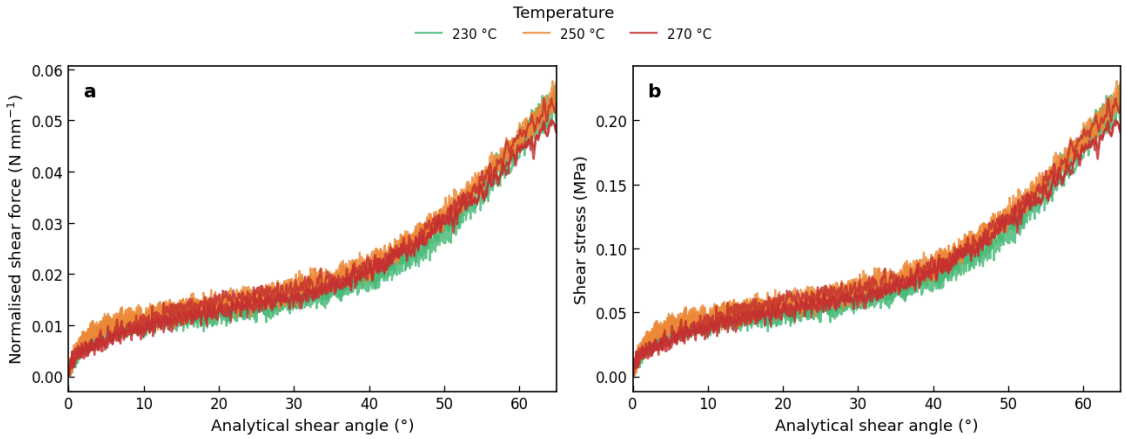


Figure 8 Molten-state shear responses of woven CF/PA6 at 230, 250 and 270 °C and 60 mm min^{-1}: (a) normalised shear force; (b) shear stress, both plotted against the analytical shear angle. Three individual specimen curves are shown for each temperature.

3.3 Effect of deformation rate on shear behaviour

Figure 9 compares the molten-state shear responses of woven CF/PA6 at 230 °C at different deformation rates. At a given analytical shear angle, increasing the deformation rate consistently increases both the normalised shear force and shear stress. The separation between the responses is evident from the early stage of deformation and increases with shear angle.

This rate dependence is consistent with previous bias-extension studies of thermoplastic composites [23, 24, 29]. Above the PA6 melting peak, the molten matrix provides viscous resistance to yarn rotation and rearrangement. At higher deformation rates, less time is available for matrix flow and relaxation, resulting in a higher shear response. These rate-dependent responses were used to calibrate the constitutive model in Section 4.

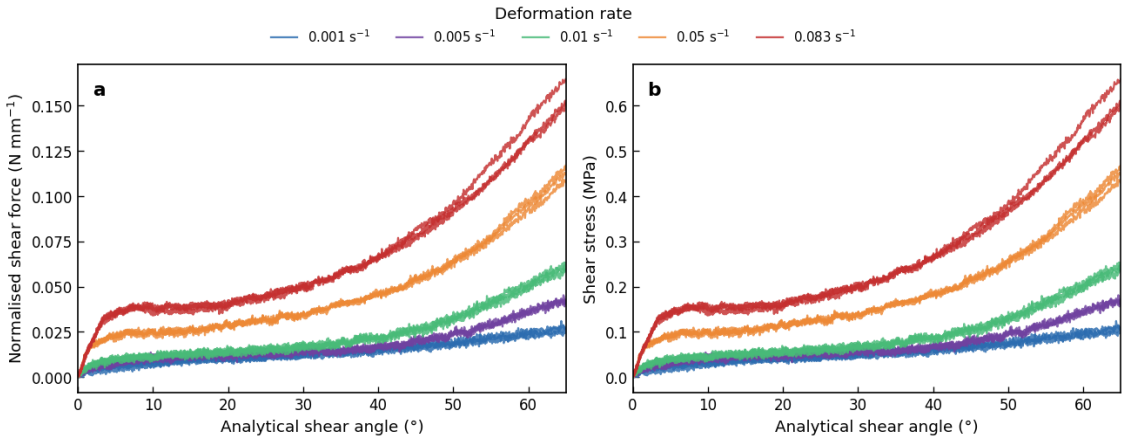


Figure 9 Rate dependence of the molten-state shear response of woven CF/PA6 at 230 °C: (a) normalised shear force; (b) shear stress, both plotted against the analytical shear angle. Three individual specimen curves are shown for each deformation rate.

4 Rate-dependent intra-ply shear model and VUMAT implementation

This section develops the rate-dependent shear model from the bias-extension results, followed by parameter identification, VUMAT implementation and the orthotropic support properties used for the remaining stress components.

4.1 Model variables and local shear rate

A rate-dependent law was developed for the in-plane 12-shear response of molten woven CF/PA6. Within the tested molten-state range, temperature produced no consistent change in the shear response, whereas deformation rate had a clear effect (Figure 9). The model was therefore formulated using shear angle and local engineering shear rate, without an explicit temperature term.

In the constitutive law, the shear angle is denoted by θ, and γ_{12} denotes the engineering 12-shear strain, with $\gamma_{12} = \tan\theta$. The local engineering shear rate, $\dot{\gamma}_{12}$, calculated from Eq. (2), is used as the rate variable. The deformation rates listed for the experiments describe the test conditions, while the local shear rate changes during loading. Angles are expressed in degrees in the constitutive functions and converted to radians for trigonometric evaluation.

A reference shear rate, $r_0 = 0.040$ s^{-1}, was used to define the dimensionless logarithmic rate variable

$$x = \ln\left(\frac{\dot{\gamma}_{12}}{r_0}\right). \tag{7}$$

Across the five loading histories, the local engineering shear rate ranged from approximately 0.004 to 0.94 s^{-1} over 0–14 mm displacement. A transition angle, $\theta_1 = 6°$, was introduced at the common change in

curvature of the five rate-dependent shear responses, separating the initial toe branch from the subsequent nonlinear hardening branch.

4.2 Two-branch rate-dependent shear law

The shear response is represented by two continuous branches connected at θ_1.

Branch I: initial toe response

For $0 \le \theta \le \theta_1$, the initial toe response is described by a saturation-type exponential function:

$$\tau(\theta, \dot{\gamma}_{12}) = \tau_p(\dot{\gamma}_{12}) \left[1 - exp\left(-\frac{\theta}{\theta_0(\dot{\gamma}_{12})}\right)\right], \quad 0 \le \theta \le \theta_1, \tag{8}$$

where τ is the shear stress in MPa, τ_p is the asymptotic shear-stress parameter in MPa, and θ_0 is the characteristic angle in degrees. Their rate dependence is defined as

$$\tau_p(\dot{\gamma}_{12}) = t_{p0} + t_{p1}x, \tag{9}$$

$$\theta_0(\dot{\gamma}_{12}) = \theta_{00} exp(\theta_{01}x), \tag{10}$$

where t_{p0} and t_{p1} are fitted stress coefficients in MPa, θ_{00} is a fitted characteristic angle in degrees, and θ_{01} is a dimensionless rate-sensitivity coefficient.

Branch II: nonlinear hardening response

For $\theta > \theta_1$, the nonlinear hardening response is described by

$$\tau(\theta, \dot{\gamma}_{12}) = \tau(\theta_1, \dot{\gamma}_{12}) + \tau_{\text{ref}}\left[k(\dot{\gamma}_{12})\Delta\bar{\theta} + C(\dot{\gamma}_{12})\Delta\bar{\theta}^{\,m(\dot{\gamma}_{12})}\right], \theta > \theta_1, \tag{11}$$

where

$$\Delta\bar{\theta} = \frac{\theta - \theta_1}{\theta_{\text{ref}}}, \qquad \theta_{\text{ref}} = 1^\circ, \tag{12}$$

with $\tau_{\text{ref}} = 1$ MPa. The rate-dependent terms are defined as

$$k(\dot{\gamma}_{12}) = \exp(k_0 + k_1 x), \tag{13}$$

$$C(\dot{\gamma}_{12}) = \exp(C_0 + C_1 x), \tag{14}$$

$$m(\dot{\gamma}_{12}) = m_0 + m_1 x, \tag{15}$$

and the exponent is bounded by

$$m_{\min} \le m(\dot{\gamma}_{12}) \le m_{\max}. \tag{16}$$

All fitted coefficients in Eqs. (13)–(15) are dimensionless. The reference angle and stress provide the scales required for dimensional consistency. The Branch II expression is anchored to $\tau(\theta_1, \dot{\gamma}_{12})$, ensuring stress continuity at θ_1; tangent continuity is not imposed.

4.3 Parameter identification and constitutive response

The constitutive law was fitted directly to the BET data before VUMAT implementation. The five molten-state datasets at deformation rates of 0.001, 0.005, 0.010, 0.050 and 0.083 s^{-1} were used for parameter identification. For each condition, Eqs. (1), (2) and (5) were used to obtain the analytical shear angle, local engineering shear rate and shear stress at each displacement sample.

A single parameter set was identified by simultaneous nonlinear least-squares fitting to the five mean shear-stress curves using the shear-angle and local shear-rate histories. Model agreement was evaluated over 0–14 mm displacement, where the measured and analytical shear-angle histories remained close.

The reference rate was fixed during fitting. The transition angle and exponent bounds were prescribed, while the remaining ten coefficients were fitted. For numerical evaluation, the local engineering shear rate was bounded between 0.004 and 1.0 s^{-1}, and the shear stress was capped at 1.2 MPa. The same bounds were used during fitting and VUMAT evaluation. The prescribed values and fitted coefficients are listed in Table 3.

Table 3 Prescribed values and fitted coefficients of the two-branch shear model.

Parameter	Value	Unit / meaning
r_0	0.040	s^{-1}, reference shear rate
θ_1	6.0	deg, transition angle
t_{p0}	0.113116	MPa, Branch I asymptotic stress at r_0
t_{p1}	0.0272522	MPa, Branch I stress rate coefficient
θ_{00}	10.3698	deg; Branch I characteristic angle at r_0
θ_{01}	-0.464922	–; Branch I angle rate coefficient
k_0	-8.01820	–; Branch II linear-amplitude log intercept
k_1	-0.834692	–; Branch II linear-amplitude rate coefficient
C_0	-20.3188	–; Branch II power-amplitude log intercept
C_1	4.54006	–; Branch II power-amplitude rate coefficient
m_0	3.33651	–; Branch II exponent at r_0
m_1	-0.716499	–; Branch II exponent rate coefficient
$m_{\min}$	1.10	–; lower exponent bound
$m_{\max}$	4.50	–; upper exponent bound

Figure 10 compares the fitted constitutive response with the experimental data over 0–14 mm displacement. Using the local engineering shear-rate histories, the pooled RMSE between the model and the five mean experimental curves was 0.0103 MPa, with a coefficient of determination of $R^2 = 0.966$. The fitted law reproduced the main rate-dependent separation and nonlinear evolution of the experimental response. The comparison is presented against both shear angle and engineering shear strain, γ_{12}.

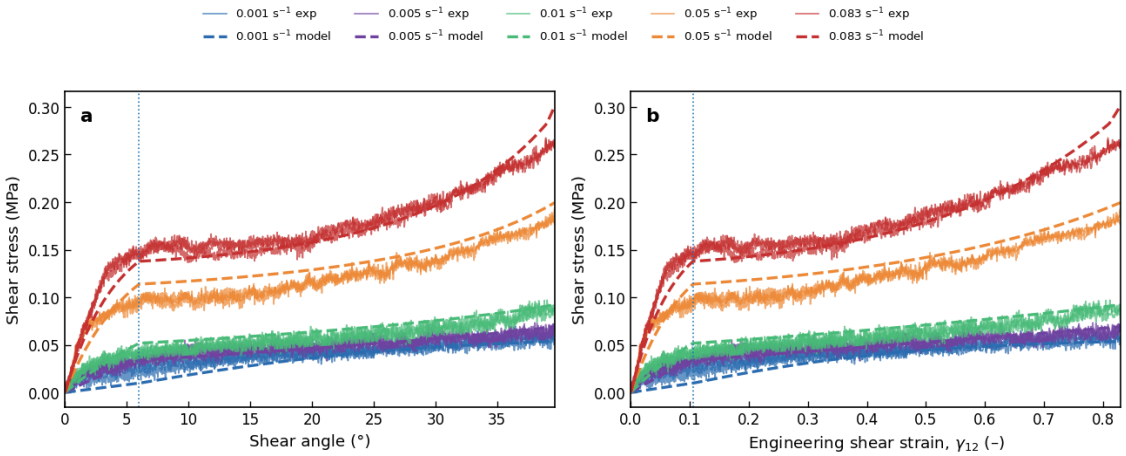


Figure 10 Experimental and model shear-stress responses over 0–14 mm displacement (analytical shear angle ≤ 39.7°) at five deformation rates (0.001–0.083 s^{-1}): (a) shear angle; (b) engineering shear strain. Solid curves show the three individual experimental responses for each condition, and dashed curves show the model responses. The vertical dotted lines mark the transition angle θ_1 and $\gamma_{12} = tan\,\theta_1$.

4.4 Three-dimensional VUMAT implementation and verification

After parameter identification, the fitted shear law was implemented in Abaqus/Explicit through VUMAT as the 12-shear response of three-dimensional solid elements, replacing the constant G_{12} response. The normal components and the 13- and 23-shear components were represented by orthotropic elastic support, while temperature was retained as a field variable in the coupled thermo-mechanical analysis.

The constitutive update is performed in the corotational material basis, with the local 1- and 2-directions initially aligned with the warp and weft directions. The basis follows the material rotation. The tensorial 12-shear increment supplied by Abaqus/Explicit is converted to engineering form as

$$\Delta\gamma_{12} = 2\Delta\varepsilon_{12}, \tag{17}$$

where $\Delta\varepsilon_{12}$ is the tensorial 12-shear strain increment supplied by Abaqus/Explicit, and $\Delta\gamma_{12}$ is the engineering shear strain increment. Both are dimensionless.

The engineering shear increments are accumulated to update γ_{12}. For the monotonic deformation considered here, the effective shear angle is calculated as

$$\theta_{12} = \tan^{-1}(|\gamma_{12}|)\frac{180}{\pi}, \tag{18}$$

where θ_{12} is the effective shear angle in degrees.

The local engineering shear rate is calculated as

$$\dot{\gamma}_{12} = \left|\frac{\Delta\gamma_{12}}{\Delta t}\right|, \tag{19}$$

where Δt is the explicit time increment in s.

The sign of the 12-shear stress is recovered from the accumulated shear strain as

$$\tau_{12} = \mathrm{sign}(\gamma_{12})\tau(\theta_{12}, \dot{\gamma}_{12}), \tag{20}$$

where $\mathrm{sign}(\gamma_{12})$ is the sign function and $\tau(\theta_{12}, \dot{\gamma}_{12})$ is the shear stress calculated from the two-branch law. The VUMAT implementation was verified using homogeneous single-element shear tests. For the five loading histories, the stresses returned by VUMAT reproduced the direct evaluation of the constitutive equations using the identified parameter set.

SDV1–SDV6 store the accumulated ε_{11}, ε_{22}, ε_{33}, γ_{12}, γ_{23} and γ_{13} components; SDV7 stores θ_{12} in degrees; SDV8 stores $\dot{\gamma}_{12}$ in s^{-1}; SDV9 stores τ_{12} in MPa; SDV10 stores accumulated 12-shear work per unit volume, W_{12}, in MPa; and SDV11 stores the active constitutive branch. The accumulated shear work is updated using the local stress-power increment as

$$W_{12}^{n+1} = W_{12}^{n} + \frac{1}{2}(\tau_{12}^{n} + \tau_{12}^{n+1})\Delta\gamma_{12}, \tag{21}$$

where superscripts n and n + 1 denote the start and end of the increment, respectively. The data flow and update sequence are summarised in Figure 11.

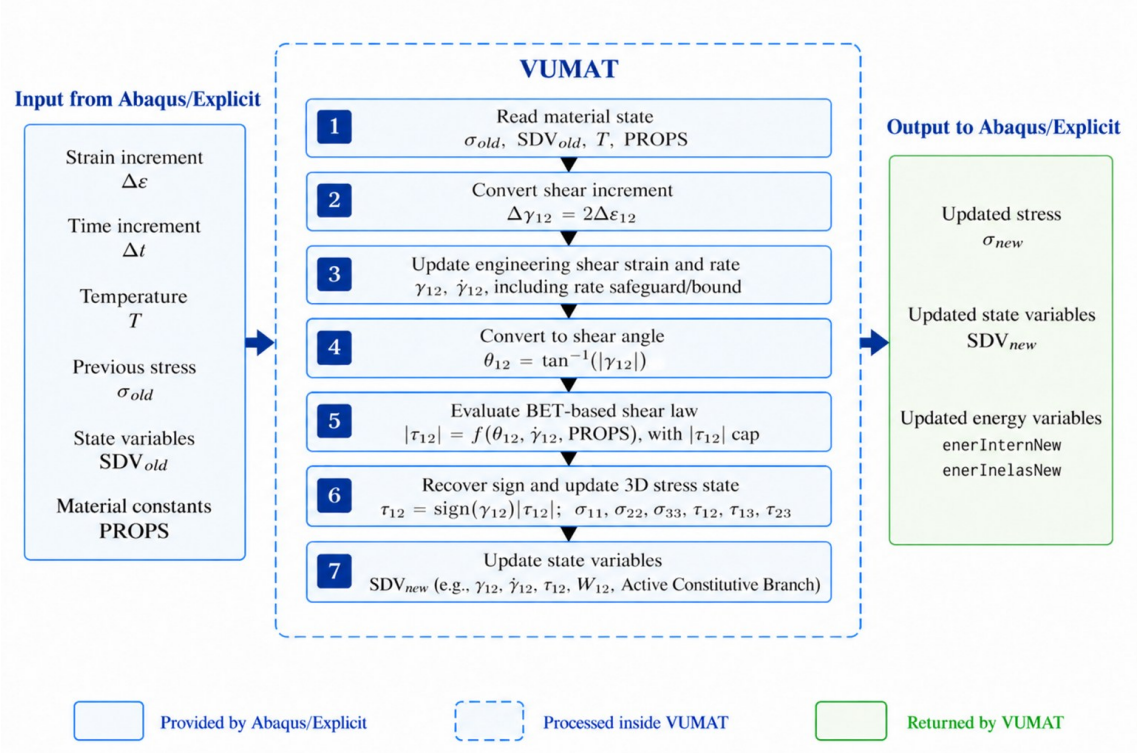


Figure 11 VUMAT update workflow for the woven CF/PA6 model. The workflow shows the engineering-shear conversion, shear-rate bounds and stress capping, stress-sign assignment, orthotropic stress update and state-variable outputs.

4.5 Orthotropic support properties

The orthotropic support properties used for the remaining stress components are listed in Table 4. Limaye et al. [30] reported an on-axis Young's modulus of 34.2 GPa at 264 °C for a balanced 2/2 twill woven CF/PA6 laminate. This value was adopted for both E_1 and E_2, aligned with the local warp and weft directions. Complete high-temperature three-dimensional elastic constants were not available for the present material, so the remaining components were assigned as engineering support properties.

The through-thickness modulus, E_3, was set to 1.71 GPa, equal to 5% of the adopted in-plane modulus. The in-plane Poisson's ratio, $\nu_{12} = 0.12$, was taken from a long-glass-fibre/PA6 composite reported in [31], while $\nu_{13} = \nu_{23} = 0.30$ were used as support values. The transverse-shear moduli, G_{13} and G_{23}, were estimated from E_3 and the associated Poisson's ratios as

$$G_{13} \approx \frac{E_3}{2(1+\nu_{13})}, \quad G_{23} \approx \frac{E_3}{2(1+\nu_{23})}. \tag{22}$$

These support properties were kept constant with temperature during the coupled analysis.

Table 4 Orthotropic elastic support properties used in the three-dimensional model.

Parameter	Value	Unit / meaning
E_1	34200	MPa; Young's modulus
E_2	34200	MPa; Young's modulus
E_3	1710	MPa; Young's modulus
ν_{12}	0.12	–; 12 Poisson's ratio
ν_{13}	0.30	–; 13 Poisson's ratio
ν_{23}	0.30	–; 23 Poisson's ratio
G_{13}	658	MPa; 13 shear modulus
G_{23}	658	MPa; 23 shear modulus

5 Application to U-shaped thermoforming and validation

The rate-dependent shear model was applied to the U-shaped forming case described in Section 2.5 using the experimental laminate architecture, tool geometry, initial temperature and mechanical conditions. Model validation was based on the overall formed geometry and yarn-angle measurements along the fixed outer-surface centreline.

5.1 Finite element model and boundary conditions

The U-shaped forming model was implemented in Abaqus/Explicit using the experimental tool geometry and forming sequence. A quarter-symmetry model represented one quarter of the 120 × 40 mm blank together with the punch, die, blank holder and spacers. Symmetry boundary conditions were applied to the

two cut planes. Because identical properties were assigned in the warp and weft directions, reflection about the two blank symmetry planes preserved the ±45° yarn architecture, allowing quarter symmetry to be used. The supplier-reported ply thickness of 0.25 mm refers to the as-received prepreg. After consolidation, the measured room-temperature thickness of the $[45°]_{15}$ laminate was 3.0 mm, giving a consolidated ply thickness of 0.200 mm. Through-thickness thermal expansion from 23 to 245 °C was calculated using $\alpha_3 = 25 \times 10^{-6}$ K^{-1}, together with a 5% allowance for thickness recovery [32]. This gave an initial hot-state ply thickness of 0.211 mm and a total laminate thickness of 3.167 mm.

The BET-derived shear-stress law, based on the 0.25 mm reference ply thickness, was assigned directly to the consolidated model plies without additional thickness rescaling. The laminate was represented by 15 individual solid plies.

Each woven ply was discretised using eight-node, reduced-integration, coupled temperature–displacement brick elements (C3D8RT), with an in-plane element size of 1 mm and one element through the thickness of each ply. A local material coordinate system was assigned to each ply, with the 1- and 2-directions initially aligned with the warp and weft yarns. The yarns were oriented at ±45° to the blank length in accordance with the experimental lay-up.

The laminate was initialised at 245 °C, while the punch, die, blank holder and spacers were initialised at 23 °C. Constant thermal contact conductances of 1 and 6 kW m^{-2} K^{-1} were assigned to the tool–ply and ply–ply interfaces, respectively. Related thermal contact modelling approaches are described in [33, 34]. Thermal expansion remained active during the coupled thermo-mechanical analysis.

The punch travelled 36.232 mm over 0.36232 s, giving a mean speed of 100 mm s^{-1}, while the die remained fixed. A blank-holder force of 15 kN was applied in the quarter model, equivalent to the experimental total force of 60 kN. After forming, the laminate was held under tool closure for 30 s.

The woven–woven and woven–tool friction responses were implemented through the VFRIC_COEF user subroutine using the experimentally calibrated interface-dependent friction definitions reported in Gao et al. [35]. These contact responses were defined separately from the intra-ply shear response implemented in the VUMAT. Fixed mass scaling was used to reduce the computational cost of the coupled explicit analysis. The total kinetic energy remained below 1% of the total internal energy throughout the forming stage.

5.2 Overall geometry and cross-sectional observations

Figure 12 compares the numerical and experimental U-shaped profiles. The profiles, shown at the same section and scale, show similar overall geometry and corner-transition locations. Representative optical cross sections from the upper-corner and mid-wall regions are included to examine the local laminate condition after forming. No obvious large voids, delamination or severe interlaminar separation are visible in these sections, and the reinforcement remains continuous through the laminate thickness. As such defects can reduce the shear performance of thermoplastic composites [36], the micrographs provide a qualitative check of the local laminate integrity in the formed component.

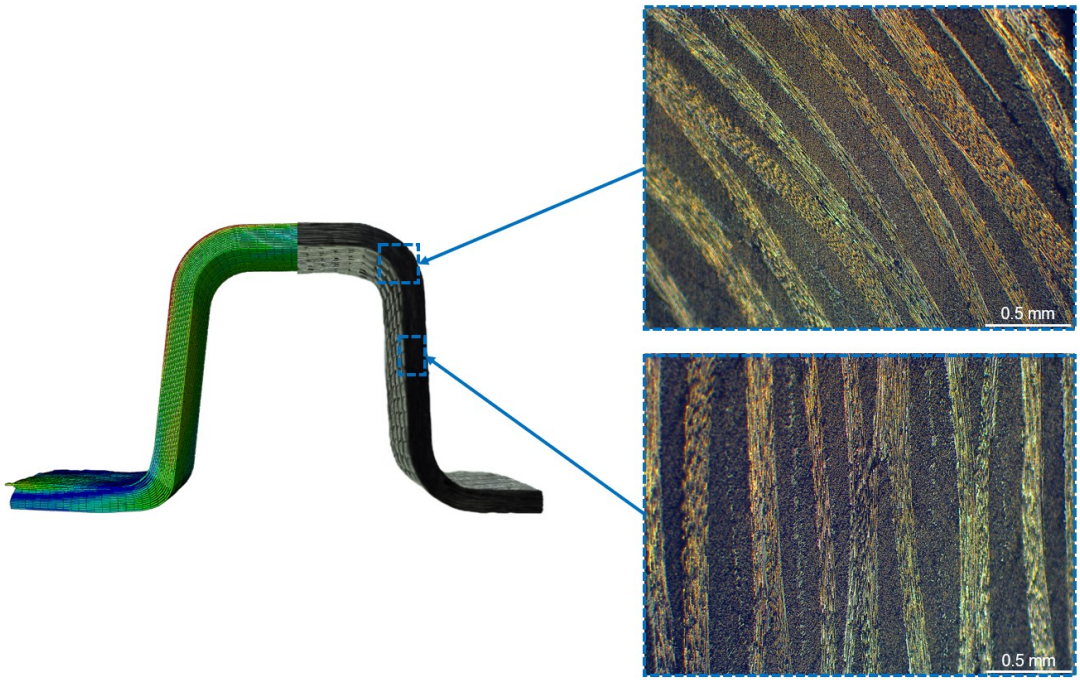


Figure 12 Numerical and experimental U-shaped profiles with representative optical micrographs from the upper-corner and mid-wall regions.

5.3 Shear-angle field and centreline comparison

Figure 13 presents the numerical shear-angle field, representative surface photographs and the centreline comparison. Experimental measurement locations were matched to positions along the numerical centreline using the component geometry. The numerical shear angle stored in SDV7 was extracted along the outermost-ply centreline at the nine measurement locations defined in Section 2.6. The mean absolute error (MAE) and root-mean-square error (RMSE) were calculated using the numerical values and the mean experimental angle at each location. Representative surface photographs at $s \approx 18$ mm and $s \approx 31$ mm illustrate the yarn-angle measurement.

The numerical shear-angle field shows higher shear around the upper-corner transition, followed by a reduction along the wall towards the lower corner and an increase towards the lower flange. The two forming tests show the same main spatial trend along the centreline.

At $s \approx 18$ mm, the measured shear angles were approximately 18° and 16°, compared with 16.32° numerically. At $s \approx 31$ mm, the experimental angles were approximately 13.6° and 13.0°, compared with 12.22° numerically. Further along the wall, at $s \approx 37$ mm, the measured values decreased to 8° and 7°, while the numerical value was 8.46°.

A larger local difference was observed near the lower-corner transition. At $s \approx 44$ mm, the two experiments gave approximately 2° and 0°, compared with 4.85° numerically. The numerical profile then decreased to 0.40° near $s = 49$ mm before increasing again towards the lower flange. At the path origin, the mean experimental angle was 7.0°, compared with 10.73° numerically.

Across the nine locations, the numerical profile gave an MAE of 1.89° and an RMSE of 2.21° relative to the mean experimental angles. The centreline shear angles remained within the range assessed in the bias-extension tests. Overall, the model reproduced the main spatial variation of yarn rotation, with larger local differences near the path origin and lower corner.

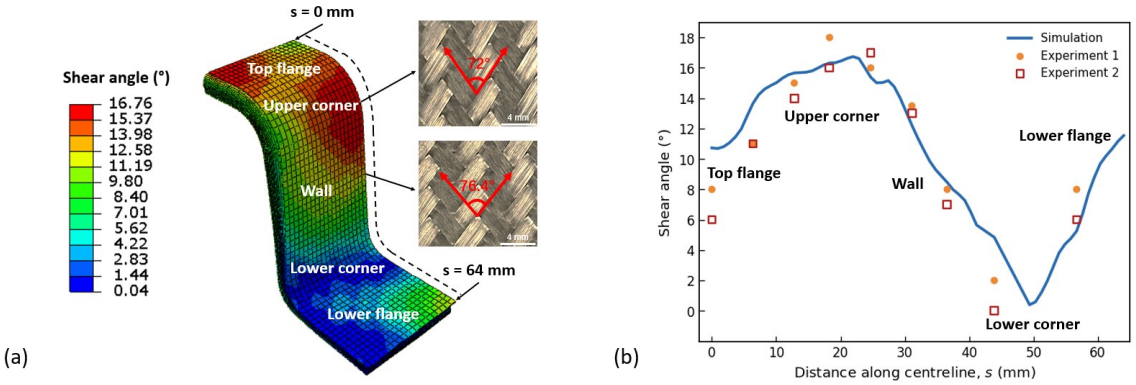


Figure 13 Forming-scale shear-angle comparison: (a) numerical shear-angle field with the centreline extraction path and representative surface photographs; the dashed path runs from s = 0 at the top flange to s = 64 mm at the lower flange; (b) numerical centreline shear-angle profile and measurements from two forming tests at nine matched locations.

6 Discussion

The experimental results define the scope of the constitutive model. Below the PA6 melting peak, the measured yarn rotation departed from the analytical bias-extension response, whereas the molten-state tests showed consistent shear kinematics and a clear dependence on deformation rate. The present model therefore focuses on the molten-state response and represents shear behaviour using shear angle and local

engineering shear rate. The relatively small variation among the tested molten-state temperatures supports the use of this rate-dependent formulation without an explicit temperature term over the present temperature range.

The U-shaped forming study assesses whether this material response can reproduce the spatial yarn rotation developed during forming. The shear angles along the assessed centreline remained within the range examined in the bias-extension tests, and the numerical profile reproduced the main variation measured along the formed component. This supports the use of the model for molten-state forming conditions within the tested shear-angle and rate ranges. The present formulation does not include a solid-state response or behaviour approaching shear locking, and the forming assessment focuses on yarn rotation rather than other outcomes such as wrinkling, springback or consolidation. Application beyond these conditions would require additional material characterisation.

7 Conclusions

This study developed a rate-dependent intra-ply shear model for molten woven CF/PA6 from bias-extension testing and validated it in U-shaped thermoforming. The main conclusions are as follows:

- Above the PA6 melting peak, the measured shear angles in region C followed the analytical BET relation closely over 0–14 mm displacement, reaching an analytical shear angle of 39.7° at 14 mm. The responses at 190 and 210 °C departed from this deformation mode.
- Within the tested molten-state range, deformation rate produced a clearer effect on the shear response than temperature. Higher deformation rates increased both the normalised shear force and shear stress.
- The continuous two-branch law reproduced the five rate-dependent shear responses over 0–14 mm displacement, with a pooled RMSE of 0.0103 MPa and $R^2 = 0.966$.
- The shear law was implemented through VUMAT as the nonlinear 12-shear response of a three-dimensional solid-element model, with orthotropic elastic support for the remaining stress components.
- In the 15-ply U-shaped forming case, the numerical model reproduced the main centreline shear-angle variation measured experimentally. Across nine measurement locations, the numerical profile gave an MAE of 1.89° and an RMSE of 2.21° relative to the mean experimental angles.

CRediT authorship contribution statement

Chunyi Gao: Conceptualization, Data curation, Formal analysis, Investigation, Methodology, Software, Validation, Visualization, Writing – original draft. **Haibao Liu:** Formal analysis, Methodology, Supervision, Writing – review & editing. **Bamber Blackman:** Supervision, Writing – review & editing. **Nan Li:** Conceptualization, Formal analysis, Funding acquisition, Methodology, Project administration, Resources, Supervision, Validation, Writing – review & editing.

Declaration of competing interests

The authors declare that they have no known competing financial interests or personal relationships that could have appeared to influence the work reported in this paper.

Data availability statement

Data will be made available on request.

Acknowledgements

Chunyi Gao acknowledges the PhD Scholarship from Imperial College London. Nan Li and Bamber Blackman would like to thank UKRI Impact Acceleration Accounts within Imperial College London (EPSRC – EP/X52556X/1). The authors thank Mr Suresh Viswanathan for his assistance with the experiments. For the purpose of open access, the authors have applied a Creative Commons Attribution (CC BY) licence to any Author Accepted Manuscript version arising.

8 References

[1] L. Zhu, N. Li, and P. R. N. Childs, "Light-weighting in aerospace component and system design," *Propulsion and Power Research,* vol. 7, no. 2, pp. 103-119, 2018, doi: 10.1016/j.jppr.2018.04.001.

[2] P. Harrison, R. Gomes, and N. Curado-Correia, "Press forming a 0/90 cross-ply advanced thermoplastic composite using the double-dome benchmark geometry," *Composites Part A: Applied Science and Manufacturing,* vol. 54, pp. 56-69, 2013, doi: 10.1016/j.compositesa.2013.06.014.

[3] B. Lv, J. Zhang, J. Xiao, S. Wang, L. Wen, and X. Hou, "Analyses of wrinkling mechanisms during forming of multi-layer woven fabric reinforced thermoplastic prepregs," *Composites Part A: Applied Science and Manufacturing,* vol. 184, Art. no. 108240, 2024, doi: 10.1016/j.compositesa.2024.108240.

[4] P. Boisse, B. Zouari, and A. Gasser, "A mesoscopic approach for the simulation of woven fibre composite forming," *Composites Science and Technology,* vol. 65, no. 3, pp. 429-436, 2005, doi: 10.1016/j.compscitech.2004.09.024.

[5] R. H. W. ten Thije and R. Akkerman, "A multi-layer triangular membrane finite element for the forming simulation of laminated composites," *Composites Part A: Applied Science and Manufacturing,* vol. 40, no. 6, pp. 739-753, 2009, doi: 10.1016/j.compositesa.2009.03.004.

[6] P. Wang, N. Hamila, and P. Boisse, "Thermoforming simulation of multilayer composites with continuous fibres and thermoplastic matrix," *Composites Part B: Engineering,* vol. 52, pp. 127-136, 2013, doi: 10.1016/j.compositesb.2013.03.045.

[7] B. Liang, N. Hamila, M. Peillon, and P. Boisse, "Analysis of thermoplastic prepreg bending stiffness during manufacturing and of its influence on wrinkling simulations," *Composites Part A: Applied Science and Manufacturing,* vol. 67, pp. 111-122, 2014, doi: 10.1016/j.compositesa.2014.08.020.

[8] C. Gao, J. Tran, Z. Ding, B. Blackman, and N. Li, "Cohesive-friction transition in compressed unidirectional thermoplastic composite interfaces," *Composites Part B: Engineering,* vol. 328, Art. no. 114187, 2027, doi: 10.1016/j.compositesb.2026.114187.

[9] J. Xie *et al.*, "Mechanics of textiles used as composite preforms: A review," *Composite Structures,* vol. 304, Art. no. 116401, 2023, doi: 10.1016/j.compstruct.2022.116401.

[10] D. Brands, W. J. B. Grouve, S. Wijskamp, and R. Akkerman, "A press forming benchmark to isolate deformation mechanisms for simulation validation," *International Journal of Material*

Forming, vol. 18, no. 2, Art. no. 27, 2025, doi: 10.1007/s12289-025-01891-x.
[11] E. Guzman-Maldonado, N. Hamila, P. Boisse, and J. Bikard, "Thermomechanical analysis, modelling and simulation of the forming of pre-impregnated thermoplastics composites," *Composites Part A: Applied Science and Manufacturing,* vol. 78, pp. 211-222, 2015, doi: 10.1016/j.compositesa.2015.08.017.
[12] H. Yin, X. Peng, T. Du, and J. Chen, "Forming of thermoplastic plain woven carbon composites: An experimental investigation," *Journal of Thermoplastic Composite Materials,* vol. 28, no. 5, pp. 730-742, 2015, doi: 10.1177/0892705713503668.
[13] S. B. Sharma, M. P. F. Sutcliffe, and S. H. Chang, "Characterisation of material properties for draping of dry woven composite material," *Composites Part A: Applied Science and Manufacturing,* vol. 34, no. 12, pp. 1167-1175, 2003, doi: 10.1016/j.compositesa.2003.09.001.
[14] Q. Chen, P. Boisse, C. H. Park, A. Saouab, and J. Bréard, "Intra/inter-ply shear behaviors of continuous fiber reinforced thermoplastic composites in thermoforming processes," *Composite Structures,* vol. 93, no. 7, pp. 1692-1703, 2011, doi: 10.1016/j.compstruct.2011.01.002.
[15] P. Harrison, M. J. Clifford, and A. C. Long, "Shear characterisation of viscous woven textile composites: a comparison between picture frame and bias extension experiments," *Composites Science and Technology,* vol. 64, no. 10, pp. 1453-1465, 2004, doi: 10.1016/j.compscitech.2003.10.015.
[16] A. G. Prodromou and J. Chen, "On the relationship between shear angle and wrinkling of textile composite preforms," *Composites Part A: Applied Science and Manufacturing,* vol. 28, no. 5, pp. 491-503, 1997, doi: 10.1016/S1359-835X(96)00150-9.
[17] P. Wang, N. Hamila, P. Pineau, and P. Boisse, "Thermomechanical analysis of thermoplastic composite prepregs using bias-extension test," *Journal of Thermoplastic Composite Materials,* vol. 27, no. 5, pp. 679-698, 2014, doi: 10.1177/0892705712454289.
[18] J. Cao *et al.*, "Characterization of mechanical behavior of woven fabrics: Experimental methods and benchmark results," *Composites Part A: Applied Science and Manufacturing,* vol. 39, no. 6, pp. 1037-1053, 2008, doi: 10.1016/j.compositesa.2008.02.016.
[19] G. Lebrun, M. N. Bureau, and J. Denault, "Evaluation of bias-extension and picture-frame test methods for the measurement of intraply shear properties of PP/glass commingled fabrics," *Composite Structures,* vol. 61, no. 4, pp. 341-352, 2003, doi: 10.1016/S0263-8223(03)00057-6.
[20] P. Boisse, N. Hamila, E. Guzman-Maldonado, A. Madeo, G. Hivet, and F. dell'Isola, "The bias-extension test for the analysis of in-plane shear properties of textile composite reinforcements and prepregs: a review," *International Journal of Material Forming,* vol. 10, no. 4, pp. 473-492, 2017, doi: 10.1007/s12289-016-1294-7.
[21] M. Machado, L. Murenu, M. Fischlschweiger, and Z. Major, "Analysis of the thermomechanical shear behaviour of woven-reinforced thermoplastic-matrix composites during forming," *Composites Part A: Applied Science and Manufacturing,* vol. 86, pp. 39-48, 2016, doi: 10.1016/j.compositesa.2016.03.032.
[22] G. E. Street and M. S. Johnson, "The intra-ply shear behaviour of non-isothermal thermoplastic composite laminates," *Journal of Composites Science*, vol. 7, no. 10, Art. no. 432, 2023, doi: 10.3390/jcs7100432.
[23] D. Zomer, S. Simaafrookhteh, K. Vanclooster, A. Dorigato, and J. Ivens, "Forming-behavior characterization of cross-ply carbon fiber/PA6 laminates using the bias-extension test," *Composites Part A: Applied Science and Manufacturing,* vol. 168, Art. no. 107436, 2023, doi: 10.1016/j.compositesa.2023.107436.
[24] R. H. Abadi, K. A. Kalteremidou, J. Karami, and D. Van Hemelrijck, "Temperature and rate dependent shear characterization and modelling of spread-tow woven Flax/PP composite laminates," *Composites Part B: Engineering,* vol. 289, Art. no. 111930, 2025, doi: 10.1016/j.compositesb.2024.111930.
[25] M. Machado, M. Fischlschweiger, and Z. Major, "A rate-dependent non-orthogonal constitutive model for describing shear behaviour of woven reinforced thermoplastic composites," *Composites Part A: Applied Science and Manufacturing,* vol. 80, pp. 194-203, 2016, doi: 10.1016/j.compositesa.2015.10.028.
[26] LANXESS Deutschland GmbH, "Tepex® dynalite 202-C200(x)/45% Carbon–PA6 Consolidated Composite Laminate," Material Data Sheet, Edition 2022-03-07.
[27] F. Härtel and P. Harrison, "Evaluation of normalisation methods for uniaxial bias extension tests on engineering fabrics," *Composites Part A: Applied Science and Manufacturing,* vol. 67, pp. 61-69, 2014, doi: 10.1016/j.compositesa.2014.08.011.

[28] P. Harrison and F. Härtel, "Correction to 'Evaluation of normalisation methods for uniaxial bias extension tests on engineering fabrics'," *Composites Part A: Applied Science and Manufacturing*, vol. 80, pp. 104–106, 2016, doi: 10.1016/j.compositesa.2015.10.013.

[29] S. P. Haanappel, R. H. W. ten Thije, U. Sachs, B. Rietman, and R. Akkerman, "Formability analyses of uni-directional and textile reinforced thermoplastics," *Composites Part A: Applied Science and Manufacturing,* vol. 56, pp. 80-92, 2014, doi: 10.1016/j.compositesa.2013.09.009.

[30] M. Limaye *et al.*, "Thermoforming process effects on structural performance of carbon fiber reinforced thermoplastic composite parts through a manufacturing to response pathway," *Composites Part B: Engineering,* vol. 235, Art. no. 109728, 2022, doi: 10.1016/j.compositesb.2022.109728.

[31] C. Gómez, D. Tobalina-Baldeon, F. Cavas, and F. Sanz-Adan, "Geometrical optimization of thermoforming continuous fibers reinforced thermoplastics with Finite Element Models: A case study," *Composites Part B: Engineering,* vol. 239, Art. no. 109950, 2022, doi: 10.1016/j.compositesb.2022.109950.

[32] C. Gröschel and D. Drummer, "The influence of moisture and laminate setup on the de-consolidation behavior of PA6/GF thermoplastic matrix composites," *International Polymer Processing,* vol. 29, pp. 660-668, 2014, doi: 10.3139/217.2976.

[33] Z. Kou, J. Xiao, D. Huan, K. Zhu, and L. Yan, "Optimization of thermal model and prediction of crystallinity during the laser-assisted tape winding process," *Journal of Reinforced Plastics and Composites,* vol. 40, no. 15-16, pp. 606-618, 2021, doi: 10.1177/0731684421992131.

[34] S. Dandangi, S. Ghanei, M. Ravandi, J. Naser, and A. Di Pietro, "Heat transfer analysis in double diaphragm preforming process of dry woven carbon fibres," *Energies,* vol. 18, no. 6, Art. no. 1471, 2025, doi: 10.3390/en18061471.

[35] C. Gao, B. Blackman, Z. Ding, and N. Li, "Isothermal and non-isothermal friction at thermoplastic composite interfaces," *Composites Part B: Engineering*, vol. 329, Art. no. 114254, 2027, doi: 10.1016/j.compositesb.2026.114254.

[36] D. Saenz-Castillo, M. I. Martín, S. Calvo, F. Rodriguez-Lence, and A. Güemes, "Effect of processing parameters and void content on mechanical properties and NDI of thermoplastic composites," *Composites Part A: Applied Science and Manufacturing*, vol. 121, pp. 308–320, 2019, doi: 10.1016/j.compositesa.2019.03.035.